

#### **PAPER**

# A generalizable new figure of merit for dose optimization in dual energy cone beam CT scanning protocols

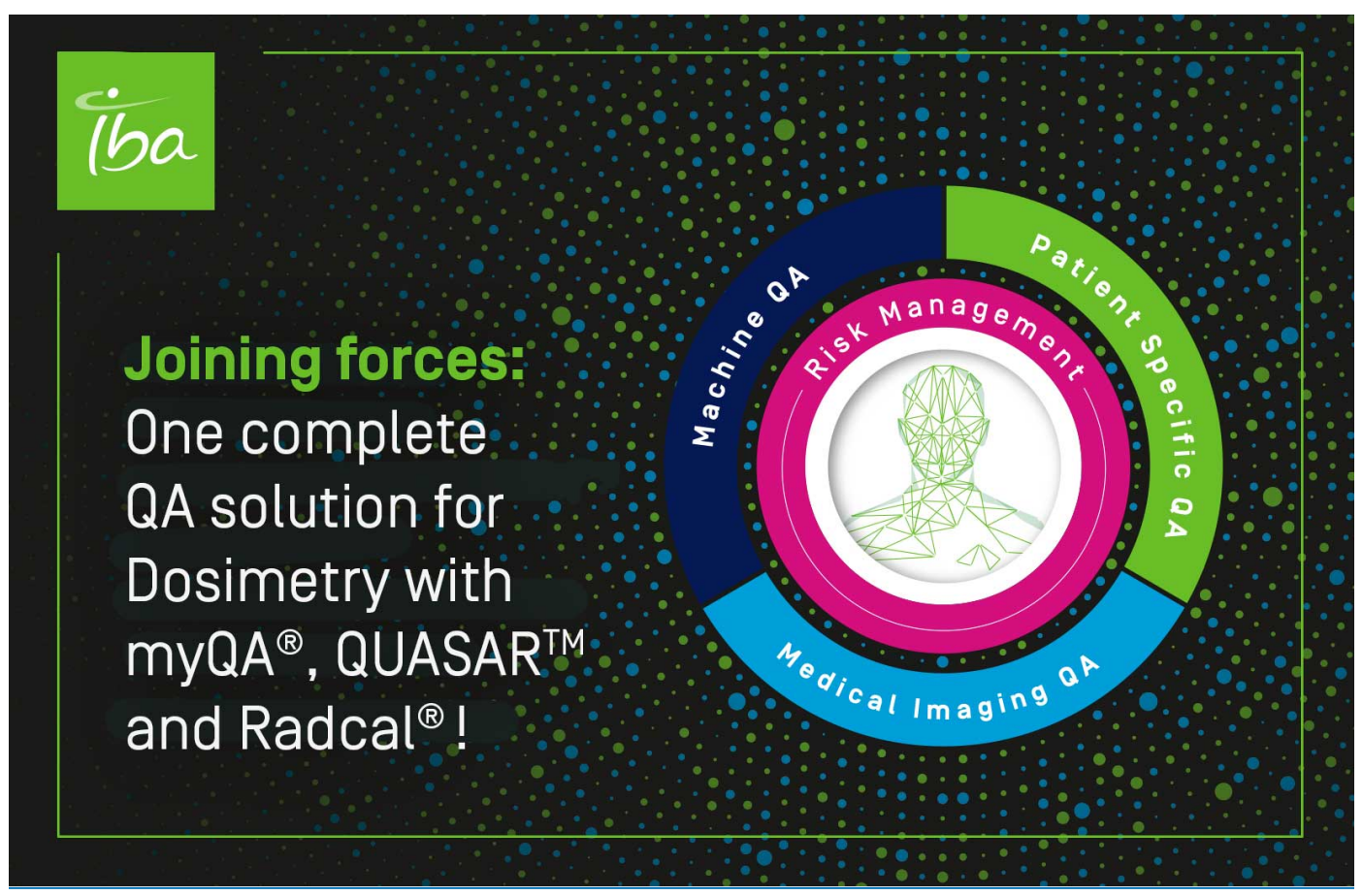
To cite this article: Chenguang Li et al 2023 Phys. Med. Biol. 68 185021

View the article online for updates and enhancements.

#### You may also like

- A nonparametric measure of contrast in xray images M Anton, M Reginatto, S Schopphoven et
- <u>Life, career, and structural biology</u>
   Yigong Shi
- LRR-CED: low-resolution reconstructionaware convolutional encoder-decoder network for direct sparse-view CT image reconstruction

V S S Kandarpa, Alessandro Perelli, Alexandre Bousse et al.



### Physics in Medicine & Biology





RECEIVED 1 May 2023

REVISED 18 August 2023

ACCEPTED FOR PUBLICATION 24 August 2023

PUBLISHED
13 September 2023

#### **PAPER**

## A generalizable new figure of merit for dose optimization in dual energy cone beam CT scanning protocols

Chenguang Li<sup>1,2,7</sup>, Li Zhou<sup>3,7</sup>, Jun Deng<sup>4</sup>, Hao Wu<sup>1</sup>, Ruoxi Wang<sup>1</sup>, Fei Wang<sup>1</sup>, Kaining Yao<sup>1</sup>, Chen Chen<sup>5</sup>, Tianye Niu<sup>6,\*</sup> and Yibao Zhang<sup>1,\*</sup>

- Key Laboratory of Carcinogenesis and Translational Research (Ministry of Education/Beijing), Department of Radiation Oncology, Peking University Cancer Hospital & Institute, Beijing, 100142, People's Republic of China
- <sup>2</sup> Department of Physics and Astronomy, University of British Columbia, 325-6224 Agricultural Road, Vancouver, BC V6T1Z1, Canada
- <sup>3</sup> Department of Radiotherapy Physics & Technology, West China Hospital, Sichuan University, No. 37 Guo Xue Xiang, Chengdu, 610041, People's Republic of China
- Department of Therapeutic Radiology, Yale University School of Medicine, New Haven, CT 06510, United States of America
- School of Electronics, Peking University, Beijing, 100871, People's Republic of China
- <sup>6</sup> Shenzhen Bay Laboratory, Shenzhen, 518118, People's Republic of China
- Chenguang Li and Li Zhou contributed equally to this work.
- \* Authors to whom any correspondence should be addressed.

E-mail: niuty@szbl.ac.cn and zhangyibao@pku.edu.cn

Keywords: dual-energy imaging, cone beam CT, scanning optimization, image wisely, image gently

#### Abstract

Objective. This study proposes and evaluates a new figure of merit (FOMn) for dose optimization of Dual-energy cone-beam CT (DE-CBCT) scanning protocols based on size-dependent modeling of radiation dose and multi-scale image quality. Approach. FOMn was defined using Z-score normalization and was proportional to the dose efficiency providing better multi-scale image quality, including comprehensive contrast-to-noise ratio (CCNR) and electron density (CED) for CatPhan604 inserts of various materials. Acrylic annuluses were combined with CatPhan604 to create four phantom sizes (diameters of the long axis are 200 mm, 270 mm, 350 mm, and 380 mm, respectively). DE-CBCT was decomposed using image-domain iterative methods based on Varian kV-CBCT images acquired using 25 protocols (100 kVp and 140 kVp combined with 5 tube currents). Main results. The accuracy of CED was approximately 1% for all protocols, but degraded monotonically with the increased phantom sizes. Combinations of lower voltage + higher current and higher voltage + lower current were optimal protocols balancing CCNR and dose. The most dose-efficient protocols for CED and CCNR were inconsistent, underlining the necessity of including multi-scale image quality in the evaluation and optimization of DE-CBCT. Pediatric and adult anthropomorphic phantom tests confirmed dose-efficiency of FOMn-recommended protocols. Significance. FOMn is a comprehensive metric that collectively evaluates radiation dose and multi-scale image quality for DE-CBCT. The models and data can also serve as lookup tables, suggesting personalized dose-efficient protocols for specific clinical imaging purposes.

#### 1. Introduction

Kilo-voltage cone-beam CT (CBCT) mounted on linear accelerators has been widely used in image-guided radiation therapy (IGRT) (Xing *et al* 2006). However, the artifacts and noise of the conventional CBCT images prevent its advanced applications to more accurate techniques such as adaptive radiotherapy (Harms *et al* 2020). Dual-energy CBCT (DE-CBCT) has been proposed as a promising solution that provides better anatomic visibility and accurate material decomposition (Sajja *et al* 2020).

Although a dedicated DE-CBCT system for IGRT has not been commercially available, several implementations have been reported by performing two-scan approaches (Men *et al* 2015, 2017), or developing novel single-scan methods (Shi *et al* 2020b, Jiang *et al* 2021, Ståhl *et al* 2021, Wang *et al* 2021). Most existing

studies have focused on the impact of new algorithms or hardware modifications on image quality (Ren *et al* 2016, Tse *et al* 2018, Skaarup *et al* 2019, Cassetta *et al* 2020, Shi *et al* 2020a, Schröder *et al* 2022), However, less attention has been paid to the scanning protocols of DE-CBCT which are more complex than those for conventional CBCT due to the increased number of possible parameter combinations involving two energies. Therefore, the definition of image quality for DE-CBCT should be more comprehensive and include the accuracy of material decomposition, in addition to conventional metrics that describe anatomic visibility, such as contrast-to-noise ratio (CNR). The figure of merit (FOM = CNR²/dose) has been widely used to assess the trade-offs between visibility and radiation dose for conventional single-energy radiography (Borg *et al* 2012, Junyu *et al* 2020). But more quality metrics than CNR need to be balanced against imaging dose for DE-CBCT, such as the accuracy of electron density (ED). Unfortunately, the present definition of FOM is not extendable to incorporate these additional metrics. Compared with the well-established dosimetric knowledge (Ding *et al* 2018), (Borg *et al* 2012) and the efficiency tools (Samei *et al* 2011) that are available for single energy modalities, the clinical experience with DE-CBCT is very limited at this preliminary stage.

To avoid unsatisfactory image quality and/or unnecessary patient exposure to radiation due to inappropriate scanning settings of DE-CBCT, it is clinically desirable to investigate the inter-correlations amongst the protocol settings, patient sizes, radiation dose, structure visibility, and accuracy of material decomposition, which have not been reported before. By modeling these correlations, this work proposed and evaluated a new figure of merit (FOMn) for DE-CBCT to balance radiation dose and multi-scale image quality including both visibility (CNR) and accuracy of material decomposition in terms of ED. The FOMn is also designed to be extendable to other multi-scale image quality parameters and other dual-energy imaging modalities such as DE-CT.

#### 2. Methods

#### 2.1. Phantoms

The Catphan604 phantom (Phantom Laboratory, NY, USA) was used to evaluate the quantitative structure visibility and the accuracy of material decomposition of DE-CBCT images. Six inserts made from Teflon, Delrin, Acrylic, Polystyrene, LDPE (low-density polyethylene), and PMP (poly(4-methyl-1-pentene)) in the Geometry and Sensitometry modules (CTP732) were analyzed. According to the manufacturer, the electron densitive relative to water of these corresponding inserts are 1.868, 1.363, 1.147, 0.998, 0.945 and 0.853, respectively.

To simulate patients of different sizes (from pediatric to obese adult patients), four in-house annuluses were made from acrylic acid which could be slipped over the PTW CTDI head phantom (PTW dosimetry company, Freiburg, Germany) or Catphan604 phantom in various combinations respectively (figure 1). The diameters of the long axis for each combination were measured as 200 mm (a), 270 mm (b), 350 mm (c), and 380 mm (d).

Two anthropomorphic phantoms of different sizes were also used to evaluate the potential clinical application of the FOMn. These phantoms included a five-year-old pediatric phantom (CIRS, Norfolk, USA) measuring 186 mm in the Left-Right direction and 145 mm in the Anterior-Posterior direction; and a RANDO adult male phantom (Alderson Research Laboratories, Stanford, USA) measuring 315 mm in the Left-Right direction and 232 mm in the Anterior-Posterior direction. These sizes were comparable to those of the Catphan604 and Catphan604+annuluses (b+c) as shown in figure 1.

#### 2.2. Imaging system and radiation dose

Based on the On-Board-Imager (OBI) system of a Varian Edge linear accelerator (Version 2.7, Varian Medical System, Palo Alto, CA, USA), CBCT images of each phantom combination were acquired at both 100 kVp and 140 kVp to have DE-CBCT images. This kVp pair was used as a methodological example for all scans in this study to demonstrate the decomposition modeling process, and other kVp pairs can be modeled using the same approach. Various mA settings and phantom sizes were combined with the two energies to quantify their impact on the radiation dose and multi-scale image quality. Specifically, the following tube currents were used as examples: 50 mA, 55 mA, 60 mA, 65 mA, and 70 mA. To maintain a large field-of-view (465.1 mm × 465.1 mm, capable of accommodating the largest phantom size), all scans were performed using the half-fan and full trajectory (360°) mode. Half bowtie, Titanium kV filter, 20 ms pulse, and 15-frame rate were used for all scanning. The iterative CBCT algorithm of the OBI system was used for image reconstruction, which can generate high-quality images with improved spatial resolution and reduced noise levels when compared to traditional reconstruction algorithms (Wang *et al* 2009).

To investigate the impact of phantom dimensions on imaging dose, a cylindrical PTW CTDI head phantom (PTW dosimetry company, Freiburg, Germany) was aligned to the CBCT iso-center indicated by the laser system, in combination with the aforementioned acrylic oval annulus of various sizes (figures 1(b)–(d)). Using the CTDI phantom along with an intermediate cylindrical acrylic adaptor would result in the same diameter as

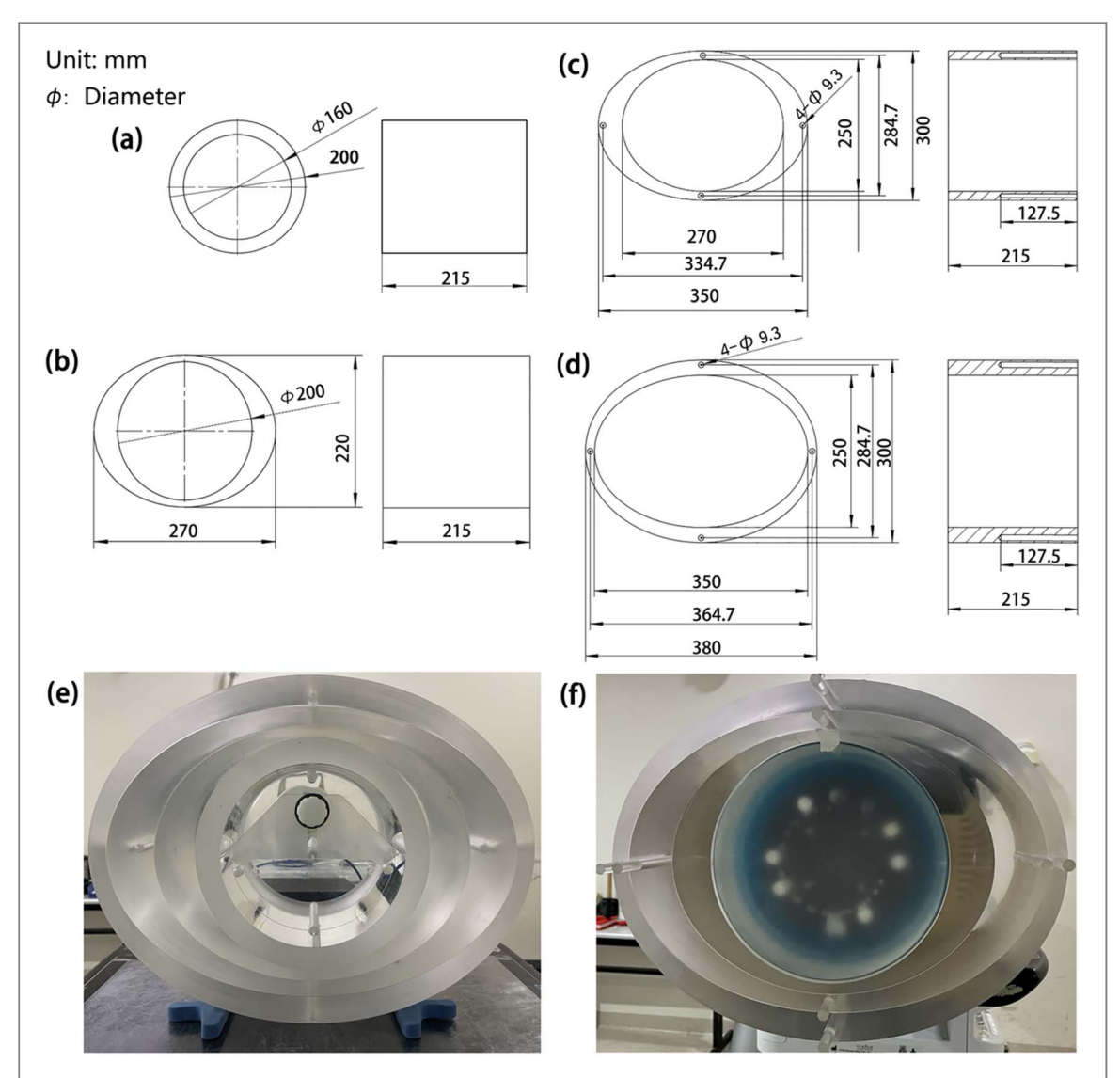


**Figure 1.** An inhouse acrylic adaptor designed to fit PTW CTDI head phantom (a). Additional oval acrylic annuluses were used to extend the phantom dimensions to simulate patients of various sizes (b)–(d). Phantom (e) combines PTW CTDI head phantom with (a), (b), (c) and (d) respectively. Phantom (f) combines Catphan604 with (b), (c) and (d) respectively.

the CatPhan604 phantom, to fit the smallest oval annulus as shown in figure 1(a). A calibrated PTW 30009 CT chamber with a length of 10 cm was connected to a PTW UNIDOS webline dosimeter to measure the doselength product (DLP) of the central hole of the CTDI phantom for each scanning protocol. Temperature and pressure corrections were applied during the measurement (Almond *et al* 1999).

#### 2.3. Calibration and decomposition

The image pixel values in Hounsfield Units (HU) were converted using HU-to-Linear Attenuation Coefficient (LAC) calibration curves to produce attenuation maps at 100 kVp and 140 kVp respectively. To produce attenuation maps, the HU-to-LAC calibration curves was generated by acquiring CBCT images of a calibration phantom containing different materials of known composition, from which the CT number (in HU) of each material could be measured. The CT number for each material was quantified as the mean CT number of a central region of interest (1.65 mm³ for the single slice). These curves were used to convert the original single-energy images in units of HU to the images in units of LAC, according to the equation (1) (Yamada *et al* 2015), in preparation for dual-energy decomposition.

$$HU_i = 1000 \left( \frac{\mu_i - \mu_{\text{water}}}{\mu_{\text{water}}} \right), \tag{1}$$

where  $\mu_i$  and  $\mu_{\text{water}}$  are linear attenuation coefficients of the measured insert and water, respectively. The image-domain iterative decomposition method proposed by Niu *et al* was used (Niu *et al* 2014). Two basis materials, Teflon and Acrylic, with LAC similar to that of bone and soft tissue, were selected, respectively. The ED of each

voxel was calculated as the sum of the two basis material images weighted by the ED of the two basis materials, respectively. For each voxel, the decomposition involved solving a system of equations with two unknowns ( $C_{\text{Teflon}}$  and  $C_{\text{Acrylic}}$ , representing the concentrations of Teflon and Acrylic) and two measurements (LAC<sub>EH</sub> and LAC<sub>EL</sub>, representing the linear attenuation coefficient at the high kVp and Low kVp, respectively), as shown in equation (2). The coefficients of the decomposition matrix ( $e_{\text{Teflon},\text{EH}}, e_{\text{Teflon},\text{EL}}, e_{\text{Acrylic},\text{EH}}, e_{\text{Acrylic},\text{EL}}$ ) were the

signal enhancement per unit concentration of two basis materials (Clark et al 2013). These coefficients were

obtained during the calibration process and remained fixed in the material decomposition

$$\begin{bmatrix} C_{Teflon} \\ C_{Acrylic} \end{bmatrix} = \begin{bmatrix} e_{Teflon,EH} & e_{Acrylic,EH} \\ e_{Teflon,EL} & e_{Acrylic,EL} \end{bmatrix}^{-1} \begin{bmatrix} LAC_{EH} \\ LAC_{EL} \end{bmatrix}.$$
 (2)

The equation (2) represents the expression for direct material decomposition, which is used as the initial solution for the iterative decomposition. Regularization term was introduced into the iterative process to enhance the smoothness of decomposed material images while maintaining boundary sharpness. More technical details of the iterative decomposition algorithm could be found in the previous publication (Niu *et al* 2014). Bone and soft tissue were utilized as the two basis materials for decomposing the anthropomorphic phantoms. Under identical scanning conditions, the high and low energy linear attenuation coefficients of the corresponding materials could be obtained in the phantoms and subsequently used for patient image decomposition.

#### 2.4. Multi-scale image quality

The central volume of 525.2 mm $^3$  (voxel size: 0.9084 mm  $\times$  0.9084 mm  $\times$  1.995 mm, 29 sampling points within the region-of-interest in each slice, 11 image slices) in each insert was selected as the volume-of-interest (VOI). The relative error of ED for each known material was calculated as:

$$RE(ED_{ij}) = \frac{|ED_{ij} - ED_{i0}|}{ED_{i0}},$$
(3)

where  $\mathrm{ED}_{ij}$  is the jth (j=1–319, Sampling points:  $29 \times 11$ ) electron density value in the ith (i=1–6, Insert rods) known material, and  $\mathrm{ED}_{i0}$  is the ground-truth electron density value provided by the manufacturer's manual of Catphan604.

The CNR of the six selected objects was calculated using the following definition, to evaluate the visibility of inserts on the DE-CBCT images of various phantom sizes and scanning protocol combinations:

$$CNR = \sqrt{\frac{2(\mu_t - \mu_b)^2}{\sigma_t^2 + \sigma_b^2}},$$
(4)

where  $\mu$  denotes the mean and  $\sigma$  denotes the standard deviation; the subscripts t and b denotes the target and the background (water equivalent material circular region around the region-of-interests) respectively. To evaluate the visual performance of DE-CBCT which is dependent on the image quality of both high and low energies, the pixel unit used in CNR calculation is ED.

#### 2.5. Theoretical definitions

To balance radiation dose and the multi-scale metrics of image quality for DE-CBCT, this work defines FOMn using Z-score normalization (Nor; Kreyszig 1979):

$$FOMn_{ij} = S \bullet Nor(I_{ij}) - Nor(Dose_{ij})$$

$$Nor(I_{ij}) = \frac{I_{ij} - \mu}{\sigma},$$
(5)

where  $\mu$  is the mean value of the  $I_{ij}$  and  $\sigma$  is the standard deviation of the  $I_{ij}$ . The target observation variables ( $I_{ij}$ ) within VOI is obtained for the ith size of phantom scanned by the jth scanning protocol. Similarly, Dose $_{ij}$  is the imaging dose to phantom i using scanning protocol j. The symbolic variable S takes a value of 1 for positive image quality metrics (higher value indicates better image quality) such as CNR. For negative metrics (higher value indicates worse image quality) such as the relative errors of ED calculated from ground truth values, the value of S is -1. This variable is employed to ensure consistency among different types of indicators.

According to the definition, higher FOMn values indicate better dose efficiency of the scanning protocol, providing better image quality in terms of CNR or ED. The performance of FOMn was evaluated on DE-CBCT images acquired from various scanning protocols combined with different phantom dimensions.

In accordance with the work of Je *et al* (2019), which described the patient material composition using combinations of various phantom insert materials, comprehensive evaluation parameter (CEP), such as the comprehensive relative error of ED (CED) or the comprehensive CNR (CCNR), is defined as:

**Table 1.** Dependence of imaging dose on the phantom sizes and scanning protocols using different combinations of tube currents and voltages (high = 140 kVp and low = 100 kVp) respectively. The unit of imaging dose is mGy. The data is rounded to one decimal place.

Phantom	Voltage	Tube current (mA)				
		50	55	60	65	70
CatPhan	High	256.8	277.3	297.1	316.1	334.8
	Low	110.6	120.5	130.0	139.6	149.0
CatPhan+Annulus1	High	206.7	223.2	238.8	254.9	270.5
	Low	84.6	92.2	99.7	107.2	114.6
CatPhanM2+Annulus2	High	154.0	166.7	179.3	191.4	203.7
	Low	60.1	65.6	71.0	76.5	81.7
CatPhanM3+Annulus3	High	115.4	125.3	135.0	144.6	154.0
	Low	43.1	47.0	51.0	55.2	59.0

$$CEP = \frac{1}{n} \bullet \left\{ P_{LD} \sum_{i=1}^{n} M_{LD,i} + P_{soft} \sum_{i=1}^{n} M_{Soft,i} + P_{HD} \sum_{i=1}^{n} M_{HD,i} \right\},$$
(6)

where  $M_{\rm LD}$ ,  $M_{\rm Soft}$ , and  $M_{\rm HD}$  represent the target physical parameters (such as the CNR or relative error of ED) of low-density structure (air-filled spaces), soft-tissue, and high-density tissue (bone) respectively.  $P_{\rm LD}$ ,  $P_{\rm Soft}$ , and  $P_{\rm hD}$  denote the composition percentages of the corresponding materials; n represents the number of sampling points.

This study categorized the six inserts into three groups: low-density structures, soft-tissue, and high-density tissue (bone). The cutoffs for these groups were set at -200 HU and 200 HU, as recommended in the work of Yang *et al* (2012). According to the typical CT number range provided in the CatPhan604 manual, PMP represented low-density structures; LDPE, Polystyrene and Acrylic represented soft tissues; Delrin and Teflon represented bone tissues. Considering the shape and dimensions of the phantoms, this study followed the material component of 'pelvis' as described in the literature (Je *et al* 2019). The relative tissue weights for 'pelvis' were: 0.5% Low-density structures (air pockets in the gastrointestinal tract), 80.2% Soft tissues, and 19.3% Bone tissues, respectively. Accordingly, CED and CCNR of the six investigated inserts were defined using equation (6) to assess the quality of DE-CBCT images more collectively.

In this study, the FOMn was used to assess the dose efficiency of each scanning protocol using multi-scale image quality defined by CED and CCNR respectively according to equation (5). The FOMn using CNR as an illustrative target parameter was benchmarked to the classic definition of FOM representing the existing clinical experience.

#### 3. Results

#### 3.1. Imaging dose

Table 1 presents the imaging dose to the central insert of the CTDI head phantom combined with the annulus of various sizes, which were used for image quality assessment. Five tube currents were combined with two tube voltages (high = 140 kVp and low = 100 kVp) to quantify the dependence of imaging dose on phantom sizes and scanning protocols, respectively.

#### 3.2. Decomposition results

Figure 2 displays the DE-CBCT images of the two basis materials: Teflon and Acrylic, respectively. As an example, the iterative decomposition results of the CTP732 module in Catphan604 and the largest size phantom (Catphan+Annulus3) are shown. The tube current used for both high and low voltages was 60 mA.

The combinations of four phantoms with 25 scanning protocols using 2 tube voltages (high = 140 kVp, low = 100 kVp) and 5 tube currents (50 mA, 55 mA, 60 mA, 65 mA, and 70 mA) yielded 100 different DE-CBCT datasets. The relative error distributions of CED are displayed in figure 3.

Using figure 3 as a lookup table, the optimal scanning protocol for a specific phantom size can be selected based on the accuracy of ED. Additionally, figure 4 displays the quantitative assessment of structure visibility in DE-CBCT images, as measured by CCNR. Images with higher CCNR values provide better image quality for clinical observation and diagnosis.

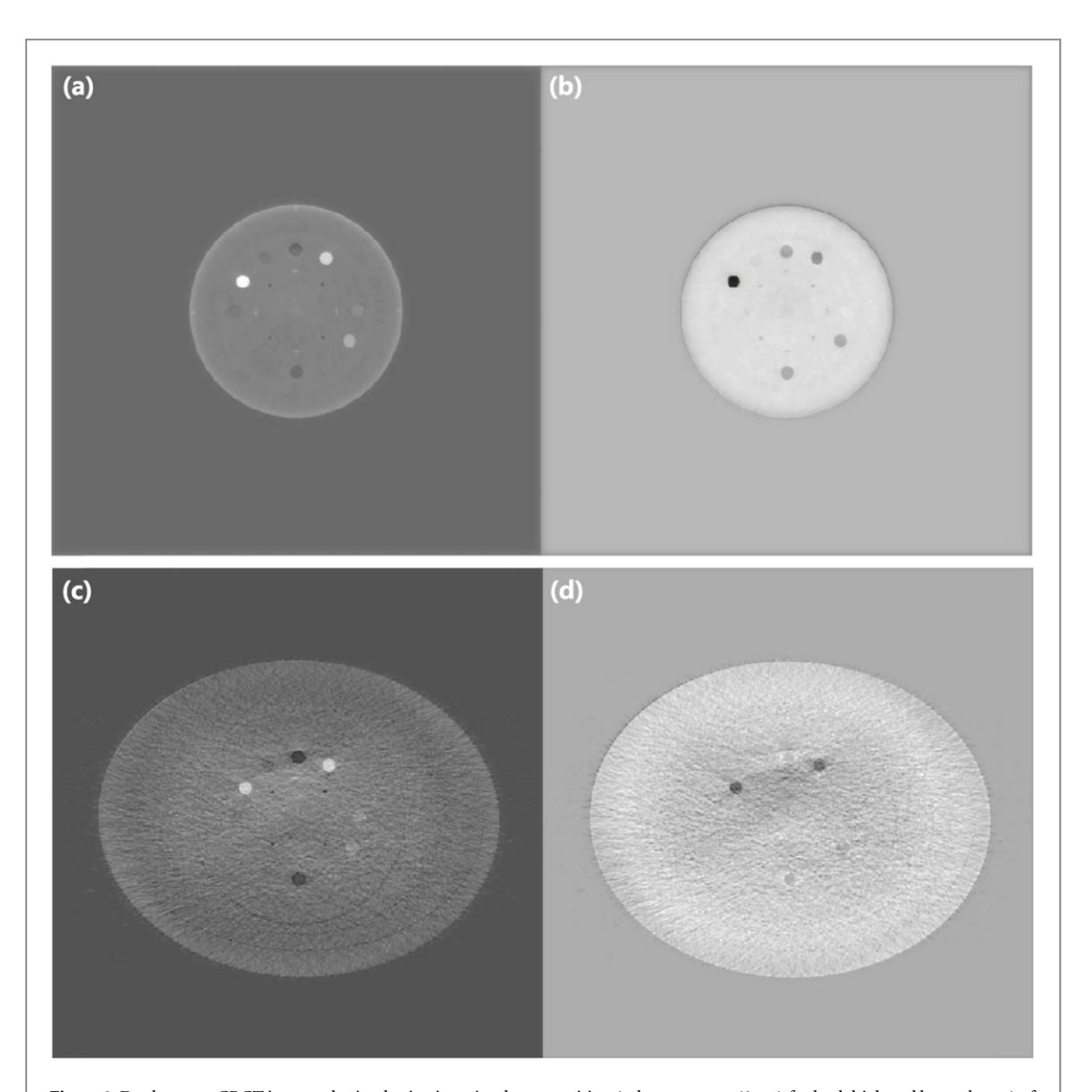


**Figure 2.** Dual-energy CBCT images obtained using iterative decomposition (tube current = 60 mA for both high and low voltages) of CTP732 module. Basis material images are displayed: (a) Teflon and (b) Acrylic images of Catphan; (c) Teflon and (d) Acrylic images of Catphan+Annulus3.

#### 3.3. Dose efficiency assessment

The results of FOMn (equation (5)) balancing the CCNR and radiation dose, are displayed in figure 5. Table 2 compares the best and worst imaging protocols based on FOMn and the classic definition of FOM (CCNR $^2$ /dose). Furthermore, figure 6 displays the FOMn results using CED as the target variable.

#### 3.4. Assessment using anthropomorphic phantoms

Based on the FOMn model for the corresponding size (figure 7(a)), the images of pediatric anthropomorphic phantom acquired using the most (figures 7(a)–(b)) and least dose-efficient protocols (figures 7(c)–(d)) were iteratively decomposed into the images of the two basis materials. Noticeable artifacts at the anterior interface between the body and air were observed on figures 7(c)–(d) using the suboptimal scanning settings, which was not a problem on figures 7(a)–(b) using the optimal protocol suggested by FOMn model. Inappropriate protocol did not only undermine the image quality of DE-CBCT, but also imposed higher radiation dose (445.4 mGy for figures 7(c)–(d)) than that of optimal protocols (405.8 mGy for figures 7(a)–(b)).

As shown in figure 8, no obvious difference was observed between the DE-CBCT images obtained using the most and least dose-efficient protocols suggested by the FOMn model based on the size of the RANDO adult phantom. In order to compare the image quality quantitatively, the image noise of the homogeneous soft-tissue was calculated as the standard deviation of ED in the central and peripheral regions of interest, as indicated by the red squares of  $20 \times 20$  pixels (330 mm<sup>2</sup>) shown in figure 8. The results of the image noise are summarized in

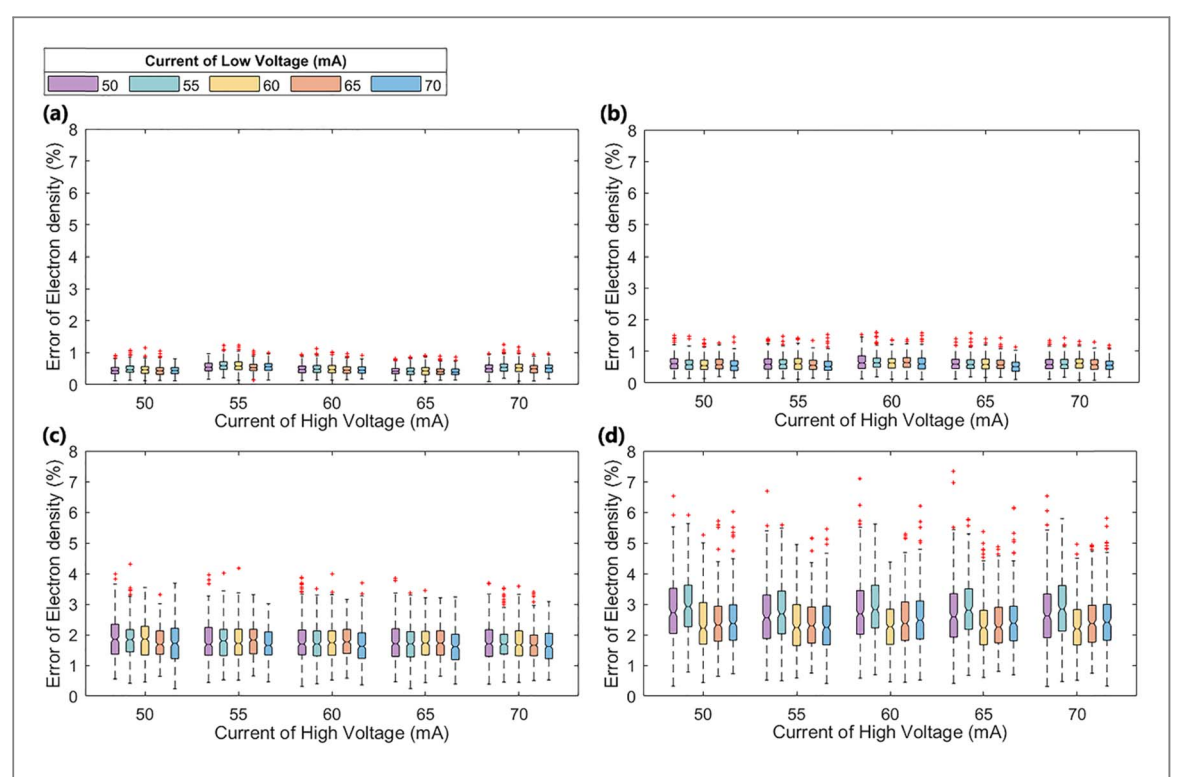
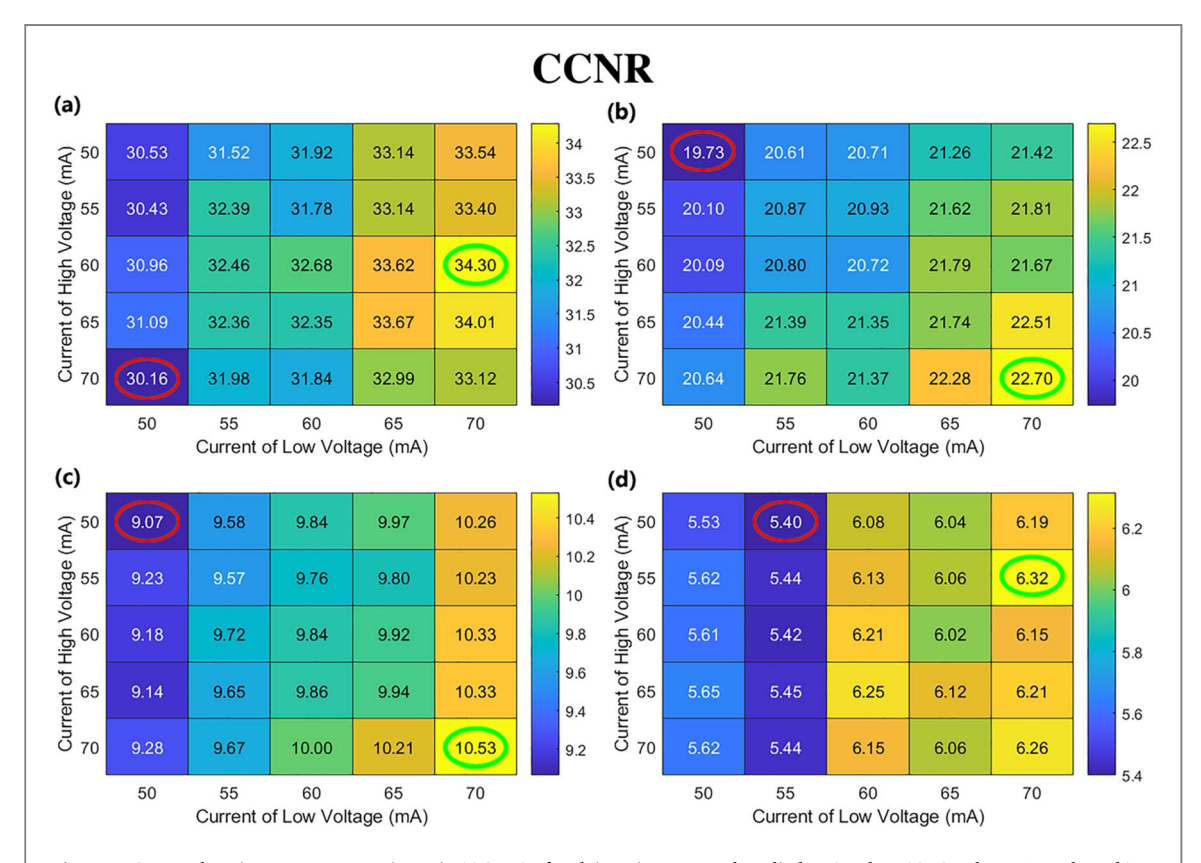


Figure 3. Absolute values of relative errors in comprehensive electron density (CED) using various combinations of tube currents (50 mA, 55 mA, 60 mA, 65 mA, and 70 mA) and voltages (high = 140 kVp and low = 100 kVp) combined with phantoms of different sizes. The subfigures (a)–(d) display the results of Catphan, Catphan+Annulus1, Catphan+Annulus2, and Catphan+Annulus3, respectively. The line in the middle of each box is the sample median; the lower and upper bounds of each box are the 25th and 75th percentiles of the sample respectively; observations beyond the whisker length (1.5 times the interquartile range) are marked as outliers.



**Figure 4.** Comprehensive contrast-to-noise ratio (CCNR) of each imaging protocol applied to Catphan (a), Catphan+Annulus1 (b), Catphan+Annulus2 (c), and Catphan+Annulus3 (d) respectively. The green and red ovals mark the best and worst protocols providing the best CCNR (highest value) and the worst CCNR respectively.

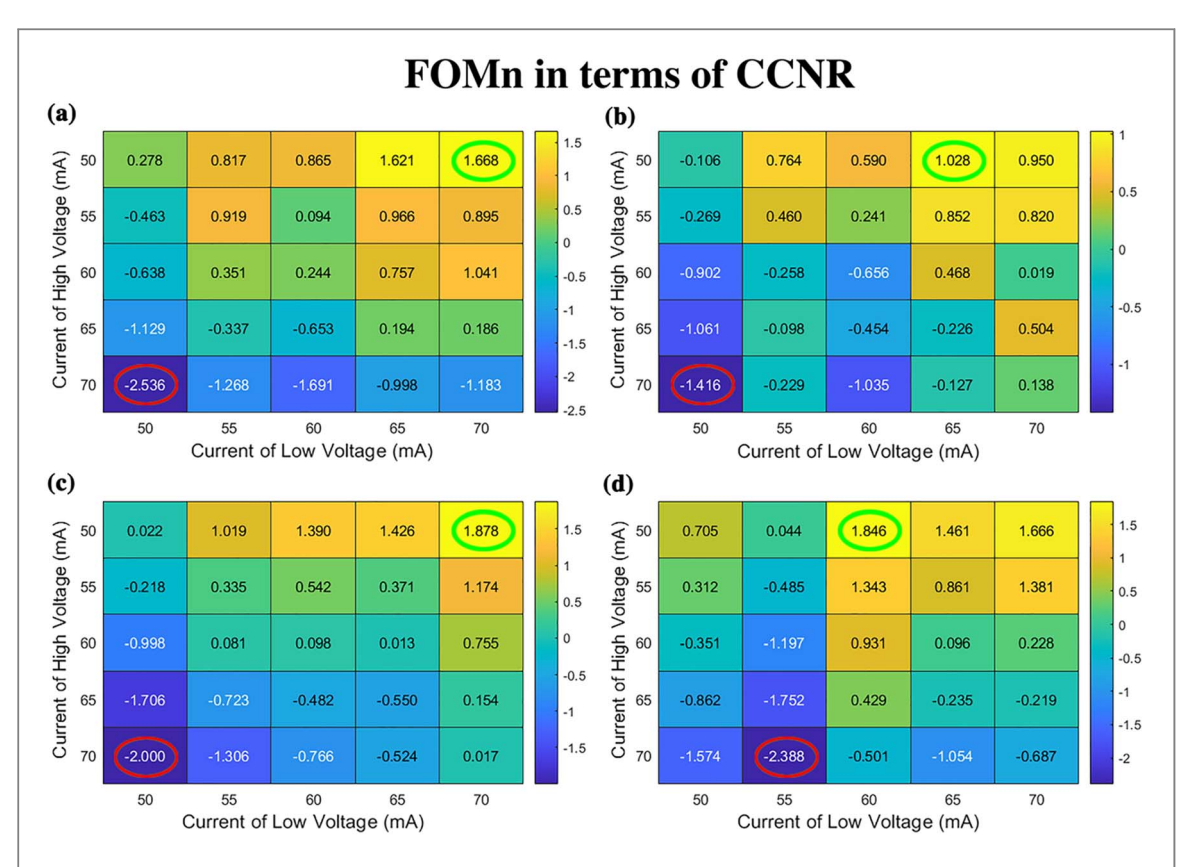


Figure 5. New figure-of-Merit (FOMn) based on comprehensive contrast-to-noise ratio (CCNR) of each imaging protocol applied to Catphan (a), Catphan+Annulus 1 (b), Catphan+Annulus 2 (c), and Catphan+Annulus 3 (d) respectively. The green and red ovals mark the most and least dose-efficient protocols considering the tradeoffs between image quality (here represented by CCNR) and radiation dose.

**Table 2.** Comparison of the best and worst imaging protocols based on the figure of merit (FOM =  $CCNR^2/dose$ ) and the new figure-of-Merit (FOMn).

	Best protocol and values		Worst protocol and values		
	FOM	FOMn	FOM	FOMn	
Catphan	140 kVp/50 mA and 100 kVp/70 mA		140 kVp/70 mA and 100 kVp/50 mA		
Catphan +Annulus1	140 kVp/ 100 kVj	2.772 1.668 140 kVp/50 mA and 100 kVp/65 mA		2.042 -2.536 140 kVp/70 mA and 100 kVp/50 mA	
Catphan +Annulus2	1.440 1.028 140 kVp/50 mA and 100 kVp/70 mA		140 kVp/ 100 kV	1.199 —1.416 140 kVp/70 mA and 100 kVp/50 mA	
Catphan +Annulus3	140 kVp/	0.446 1.878 140 kVp/50 mA and 100 kVp/60 mA 0.222 1.846		0.326 -2.000 140 kVp/70 mA and 100 kVp/55 mA 0.147 -2.388	

table 3. The optimal protocol suggested by the FOMn model provided images with lower noise and reduced radiation dose (235.72 mGy) compared to the inappropriate protocol settings (263.78 mGy).

#### 4. Discussion

The advanced applications of DE-CBCT images such as online delineation and dose calculation, rely heavily on the structure visibility and accuracy of material decomposition, which is partially determined by the scanning parameters. However, compared with single-energy CBCT, the interactions between protocol parameters, radiation dose, phantom dimension, structure visibility, and decomposition accuracy are more complex for DE-

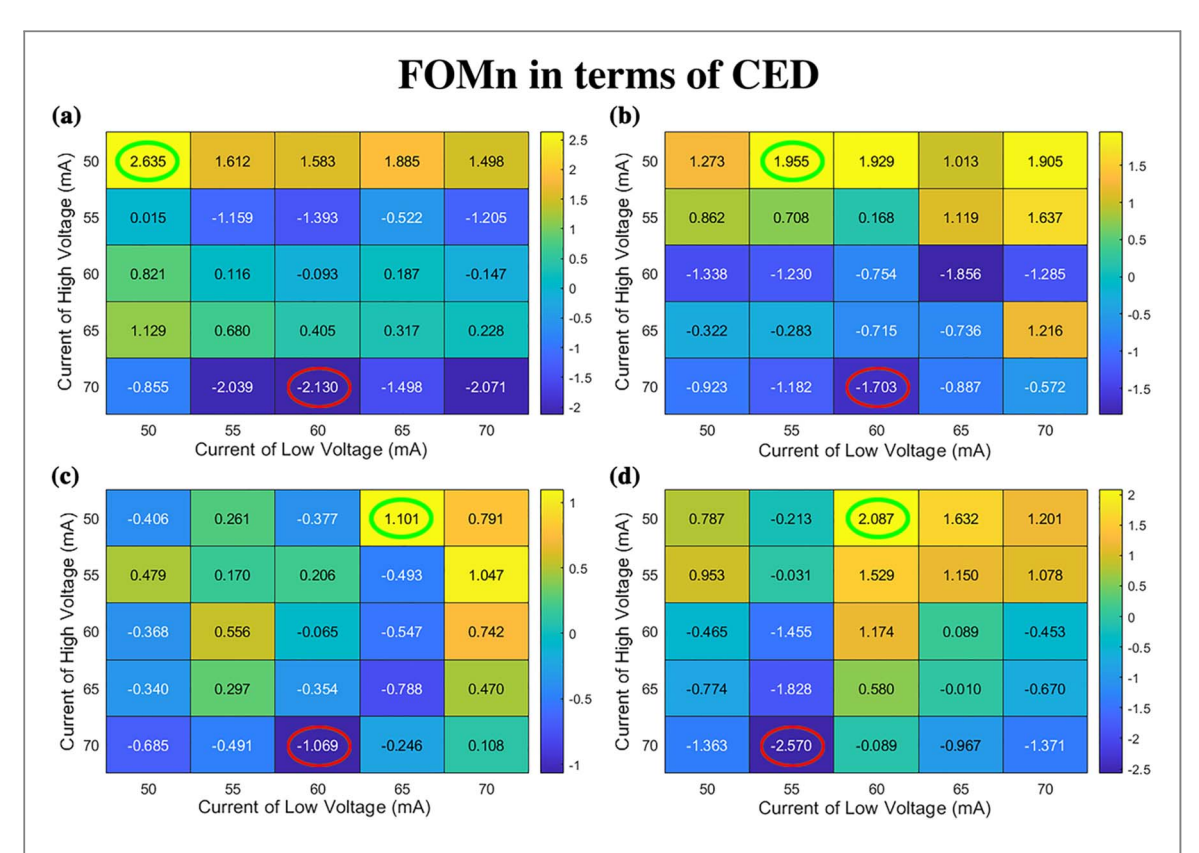
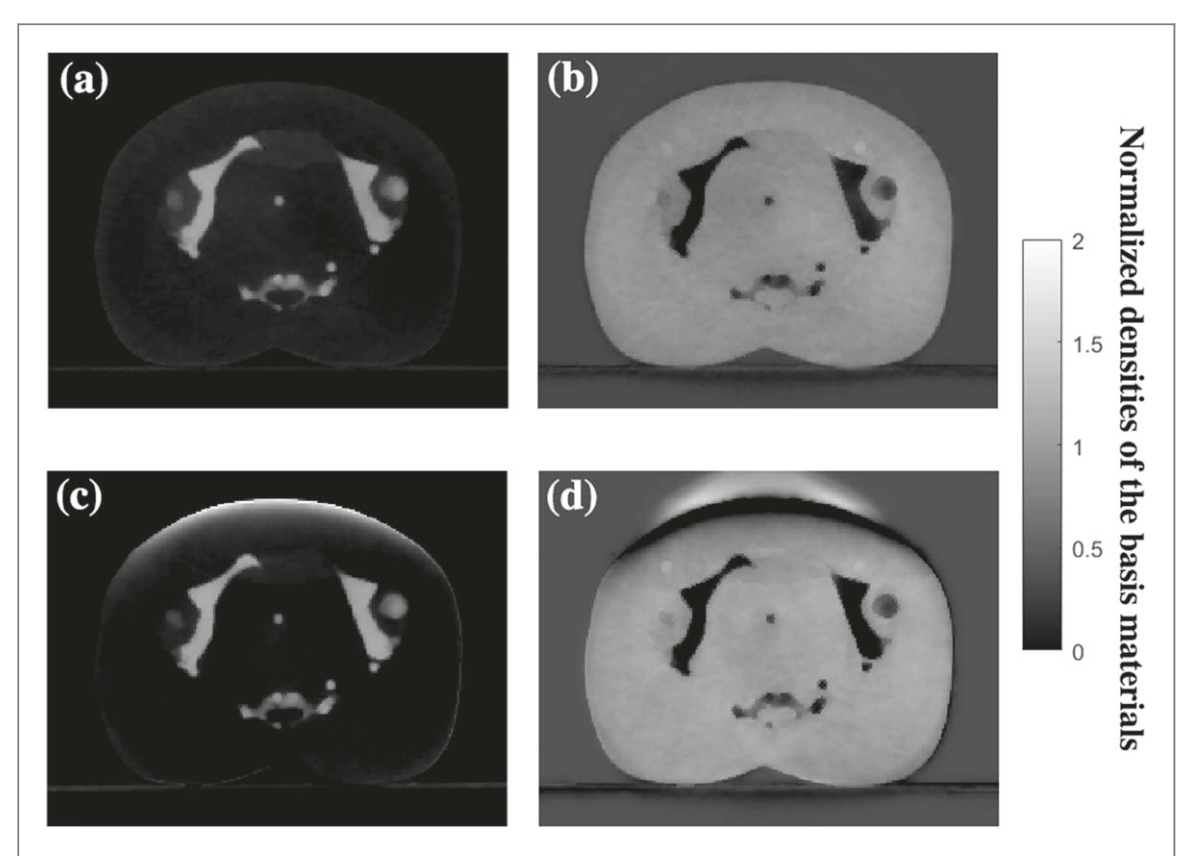


Figure 6. New figure-of-Merit (FOMn) based on relative error of comprehensive electron density (CED) of each imaging protocol applied to Catphan (a), Catphan+Annulus 1 (b), Catphan+Annulus 2 (c), and Catphan+Annulus 3 (d) respectively. The green and red ovals mark the most and least dose-efficient protocols considering the tradeoffs between image quality (CED) and radiation dose.

CBCT and have not been systematically investigated in the literature. The classic definition of FOM balancing the CNR and radiation dose for conventional single energy imaging needs to be extended to evaluate the multiscale image quality metrics of DE-CBCT such as ED. This study provided complementary methods and quantitative evidence to the limited clinical experience of DE-CBCT applied to IGRT at the early stage. This is not only beneficial to the optimal protocol selection based on present CBCT system using the double-scan technique but also aids in the protocol development of dedicated single-scan DE-CBCT systems (Xue *et al* 2021).

It should be noted that the simplified modeling of imaging dose aims to demonstrate relative correlations rather than indicating absolute organ dose. Providing the intensity of Compton scattered photons is directly proportional to the ED, it is clinically desirable to acquire accurate ED information from DE-CBCT images for the dose calculation, especially in advanced application scenarios such as adaptive radiotherapy or online treatment planning (Bernchou et al 2021). As shown in figure 3, all 25 tested imaging protocols can provide fairly accurate values of ED with relative errors of approximately 1% for small phantoms (a)–(b). According to the recommendations of the AAPM TG-65 (Papanikolaou et al 2004), the relative error of 2% to the local dose can be tolerated. Regarding the relative error of ED, the tolerance levels recommended by Nakao et al (2018) were 5.3% (low-density structure), 2.6% (soft tissue), 5.3% (bone) for 6MV photon beam, and 4.4% (low-density structure), 2.2% (soft tissue), 4.4% (bone) for 6MV flattening-filter-free (FFF) photon beam respectively. According to the aforementioned proportion of pelvis components (Je et al 2019), the CED tolerance levels should be 3.1% for 6MV beam and 2.6% for 6MV FFF beam respectively. Therefore, the relative error of ED for Catphan (figure 3(a), diameter = 200 mm) and Catphan+Annulus1 (figure 3(b), diameter = 270 mm) could meet the clinical requirements respectively. More than 75% of sampled voxels from CatPhan+Annulus2 could meet such requirements (figure 3(c), diameter = 350 mm). However, for CatPhan+Annulus3 (figure 3(d), diameter = 380 mm), the relative error of ED would be out of tolerance especially when low tube currents were used. Considering the present commissioning and quality assurance protocols of imaging devices for IGRT (including but not limited to planning CT and CBCT) are largely dependent on Catphan without extra annulus, our results suggested that the dependency of ED accuracy on patient sizes should be carefully evaluated and corrected when necessary, especially for large patients with a diameter greater than 270 mm treated with more accurate techniques such as adaptive radiotherapy.

The accuracy of ED was found to be less affected by scanning parameters as compared to its dependence on phantom sizes. Figure 3 shows that the fluctuations (standard deviations) of median values for the 25 protocols were only 0.056%, 0.034%, 0.071%, and 0.230% for the four phantoms of different sizes, respectively.



**Figure 7.** DECBCT images of the CIRS 5 year pediatric phantom iteratively decomposed into bone (first column, (a) and (c)) and soft tissue (second column, (b) and (d)) material pairs respectively. Subfigures (a)—(b) were acquired using the most dose-efficient protocol (50 mA and 70 mA for high and low voltages respectively) suggested by FOMn model based on the phantom size. Subfigures (c)—(d) were acquired using the least dose-efficient protocol (70 mA and 50 mA for high and low voltages respectively) suggested by FOMn model based on the phantom size.

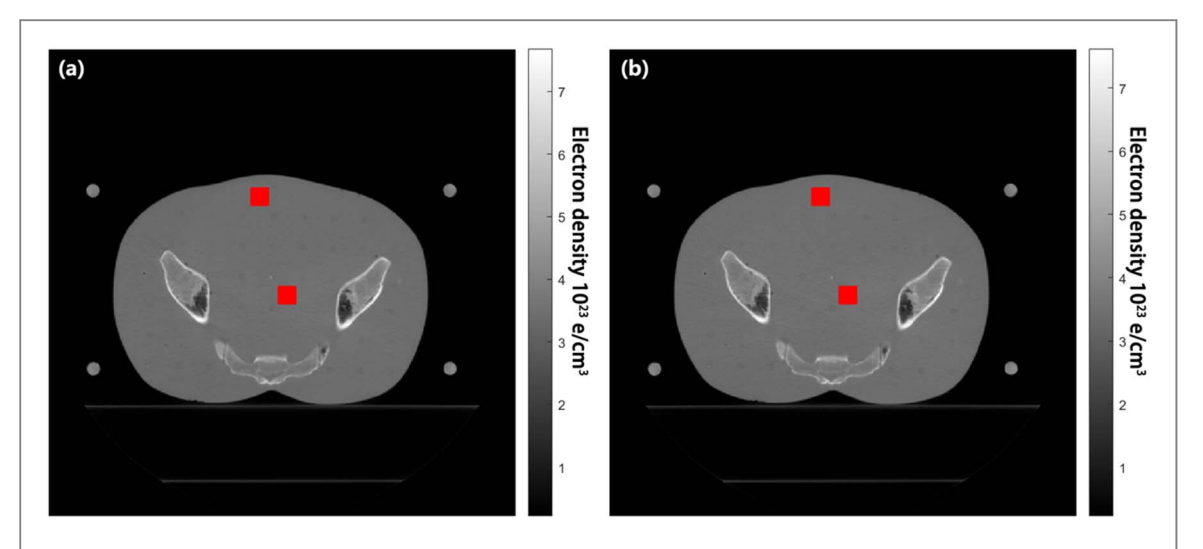


Figure 8. Iterative decomposition of DE-CBCT images of the RANDO adult phantom. Subfigure (a) was acquired using the most dose-efficient protocol (50 mA and 70 mA for high and low voltages respectively). Subfigure (b) was acquired using the least dose-efficient protocol (70 mA and 50 mA for high and low voltages respectively). The red squares of  $20 \times 20$  pixels indicate the central and peripheral regions of interest that were selected for image noise calculation in the homogeneous soft tissue.

Therefore, there is potential for dose reduction by using relatively lower mA settings without compromising ED accuracy, especially when the main clinical goal of scanning DE-CBCT is to obtain accurate ED. This can be particularly beneficial for pediatric patients with higher radiobiological sensitivity (Zhang *et al* 2012b), or if accumulated imaging dose is a risk concern when DE-CBCT is scanned frequently.

In addition to ED, structure visibility is another important metric for DE-CBCT image quality. Figure 4 can be used as a look-up table for the size-specific optimal protocol selection providing the best CCNR (indicated by

**Table 3.** Image noise of DE-CBCT images acquired using the most and least dose-efficient protocols respectively, as suggested by the FOMn model based on the size of RANDO adult phantom. The most dose-efficient protocol: 50 mA and 70 mA for high and low voltages respectively. The least dose-efficient protocol: 70 mA and 50 mA for high and low voltages respectively. The values presented in this table are expressed in electron density units (10<sup>23</sup> e cm<sup>-3</sup>).

Scanning Protocols	Central	Peripheral	
Most dose-efficient	0.044	0.028	
Least dose-efficient	0.051	0.032	

the green circles in figure 4). It was observed that the DE-CBCT image quality was not always proportional to the radiation dose, i.e. the best visibility was not always achieved by the highest combinations of kVp and mA, which are located at the lower-right corner of the matrix. The smallest and largest phantoms are the exceptions, where the optimal protocols are located at the middle-upper on the right column, suggesting the importance of patient-specific protocol optimization for DE-CBCT to avoid unexpected imaging failures due to over-exposure or insufficient signals. Basically, higher CCNR values are observed for those protocols using higher mA+lower kVp located at the right columns of the matrix, regardless of its combinations with higher kVp settings.

Similar to single energy CBCT (Zhang et al 2012a, 2015), the radiation dose of DE-CBCT is determined by both object sizes and scanning parameters. However, the numerous mA combined with two energies make it more complex to model their interactions with multi-scale image quality. Therefore, it is clinically desirable to balance the trade-offs between radiation dose and image quality, ideally in a patient-specific way. Using CCNR as a conventional definition of image quality, the locations of the most and least dose-efficient protocols suggested by FOM and FOMn are highly consistent for all phantom sizes, as shown in figure 5 and table 2. More dose-efficient protocols are those that combine higher mA+lower kVp and lower mA+higher kVp, i.e. at the upper-right/upper-middle of the heatmap matrix. On the contrary, the combination of higher mA+higher kVp and lower mA +lower kVp should be avoided in the clinical application or technical development of DE-CBCT, which provides the worst dose efficiency for phantoms of all sizes (marked by red ovals at the lower-left corner in figures 5 and 6). The most and least dose-efficient protocols for CED as shown in figure 6 is different from that of CCNR, suggesting that parameter optimization of DE-CBCT is dependent on the specific imaging purpose, as DE-CBCT could provide more information than single-energy CBCT.

As shown in figure 7 and table 3, the preliminary application of FOMn models to the pediatric and adult anthropomorphic phantoms can achieve better image quality with lower radiation dose. In addition to CCNR in the classic definition of FOM, FOMn could incorporate multi-scale image quality metrics such as CED in the dose-efficiency assessment, hence is more applicable to dual-energy imaging modalities.

For Varian CBCT system, it takes 1 min to acquire all projections for half-fan scanning using one energy setting. After waiting for about 1 min of reconstruction, CBCT using the other energy was acquired, which largely prevented ghosting artefacts due to potential over-exposure of the CBCT panel due to the adjacent two acquisitions. It is necessary to control unexpected patient motion during the time intervals to reduce image blurring. However, for regions with respiratory motion, the single scan technique such as dual-layer detector should be developed for better alignment. Focusing on the scanning protocol optimization, this work can be beneficial to the development of both single-scan and double-scan techniques.

This work aimed to optimize scanning protocols for DE-CBCT by balancing radiation dose and multi-scale image quality, which complements previous low-dose attempts using novel algorithms (Zbijewski *et al* 2013) or hardware innovations such as multi-slit beam-filter (Lee *et al* 2017), carbon nanotube (CNT) x-ray source (Li *et al* 2022), filters of various materials (Iramina *et al* 2018), and dual-layer detector (Shi *et al* 2020b), etc. The protocol optimization might be used in combination with the new algorithm and hardware to further improve the dose efficiency of DE-CBCT, which is worthy of more studies in the future.

It is worth noting that the inserts of air, bone 20% and bone 50% of Module CTP732 in CatPhan604 were not included in this study. The low ED of air (reference value:  $0.004 \times 10^{23}$  e cm $^{-3}$ ) makes it very sensitive to the image noise and artifacts in CBCT scanning, but its good contrast allows for automatic segmentation and accurate ED value assignment. In addition, the version of our OBI system was designed for Catphan504, where the new objects in Catphan604, bone 20% and bone 50%, could not be included for the HU-to-LAC calibration.

Moreover, the proportional weights in the calculation of CED and CCNR can be modified according to the patient region (Yang *et al* 2012), and the weighting coefficients of the observation quantities and dose in equation (5) can be adjusted according to the specific clinical purpose. Finally, since this study is based on Varian

TrueBeam CBCT system, the results obtained by other platforms (such as Elekta linac) may differ and require further investigation in future studies.

#### 5. Conclusions

Based on phantoms of various sizes, this work modeled the impact of scanning protocols on radiation dose, CCNR and CED for DE-CBCT. FOMn was proposed as an extendable optimizer balancing the radiation dose against multi-scale image quality.

#### Acknowledgments

The authors thank Liangzi Qu from Hebei Medical University, Yabing Gan and Guoxing Yin from Hunan Normal University, Yi Xue from Tianjin Medical University for their kind assistance.

#### Data availability statement

The data cannot be made publicly available upon publication due to legal restrictions preventing unrestricted public distribution. The data that support the findings of this study are available upon reasonable request from the authors.

#### **Funding**

This work was jointly supported by National Natural Science Foundation of China (11905150, 12275012, 62301010); Beijing Natural Science Foundation (Z210008); Peking University Emerging Engineering Interdisciplinary Project/the Fundamental Research Funds for the Central Universities (PKU2022XGK006); Project 2020BD029 supported by PKU-Baidu Fund; Science Foundation of Peking University Cancer Hospital (2021-1, PY202305, PY202306); Peking University Health Science Center Medical Education Research Funding Project (2020YB34); Open Project funded by Key Laboratory of Carcinogenesis and Translational Research, Ministry of Education/Beijing (2022 Open Project-2); National Key R&D Program of China (2019YFF01014405); Inner Mongolia Science & Technology Project Plan (2022YFSH0064).

#### **ORCID iDs**

Tianye Niu https://orcid.org/0000-0003-4181-3641 Yibao Zhang https://orcid.org/0000-0003-3658-0687

#### References

Almond P R, Biggs P J, Coursey B M, Hanson W F, Huq M S, Nath R and Rogers D W O 1999 AAPM's TG-51 protocol for clinical reference dosimetry of high-energy photon and electron beams *Med. Phys.* 26 1847–70

Bernchou U et al 2021 End-to-end validation of the geometric dose delivery performance of MR linac adaptive radiotherapy Phys. Med. Biol. 66 045034

Borg M, Badr I and Royle G J 2012 The use of a figure-of-merit (FOM) for optimisation in digital mammography: a literature review *Radiat*. Prot. Dosim. 15181–8

Cassetta R et al 2020 Fast-switching dual energy cone beam computed tomography using the on-board imager of a commercial linear accelerator Phys. Med. Biol. 65 15013

Clark D P, Ghaghada K, Moding E J, Kirsch D G and Badea C T 2013 *In vivo* characterization of tumor vasculature using iodine and gold nanoparticles and dual energy micro-CT *Phys. Med. Biol.* 58 1683–704

Ding G X, Alaei P, Curran B, Flynn R, Gossman M, Mackie T R, Miften M, Morin R, Xu X G and Zhu T C 2018 Image guidance doses delivered during radiotherapy: quantification, management, and reduction: report of the AAPM therapy physics committee task group 180 Med. Phys. 45 e84–99

Harms J, Lei Y, Wang T, McDonald M, Ghavidel B, Stokes W, Curran W J, Zhou J, Liu T and Yang X 2020 Cone-beam CT-derived relative stopping power map generation via deep learning for proton radiotherapy *Med. Phys.* 47 4416–27

Iramina H, Hamaguchi T, Nakamura M, Mizowaki T and Kanno I 2018 Metal artifact reduction by filter-based dual-energy cone-beam computed tomography on a bench-top micro-CBCT system: concept and demonstration *J. Radiat. Res.* 59 511–20

Je E, Lee H H, Duan X, Li B, Jia X and Yang M 2019 Optimal energy selection for proton stopping-power-ratio estimation using dual-energy CT-based monoenergetic imaging *Phys. Med. Biol.* 64 195015

Jiang X, Fang C, Hu P, Cui H, Zhu L and Yang Y 2021 Fast and effective single-scan dual-energy cone-beam CT reconstruction and decomposition denoising based on dual-energy vectorization *Med. Phys.* 48 4843–56

- Junyu L, Hao W, Jingxian Y, Tintin L, Songmao Y, Zihong L, Meijiao W, Chenguang L, Weibo L and Yibao Z 2020 Evaluation of cost-effective ratio (imaging quality vs. radiation dose) of Varian cone beam CT based on figure of merit (FOM) Chin. J. Radiol. Med. Prot. 40 595–9
- Kreyszig E 1979 Advanced Engineering Mathematics (Hoboken, New Jersey, USA: John Wiley and Sons Ltd) 4th edn
- Lee D, Lee J, Kim H, Lee T, Soh J, Park M, Kim C, Lee Y J and Cho S 2017 A feasibility study of low-dose single-scan dual-energy cone-beam CT in many-view under-sampling framework *IEEE Trans. Med. Imaging* 36 2578–87
- Li B, Spronk D, Luo Y, Puett C, Inscoe C R, Tyndall D A, Lee Y Z, Lu J and Zhou O 2022 Feasibility of dual-energy CBCT by spectral filtration of a dual-focus CNT x-ray source PLoS One 17 e0262713
- Men K, Dai J, Chen X, Li M, Zhang K and Huang P 2017 Dual-energy imaging method to improve the image quality and the accuracy of dose calculation for cone-beam computed tomography *Phys. Med.* 36 110–8
- Men K, Dai J-R, Li M-H, Chen X-Y, Zhang K, Tian Y, Huang P and Xu Y-J 2015 A method to improve electron density measurement of cone-beam CT using dual energy technique Bio. Med. Res. Int. 2015 858907
- Nakao M et al 2018 Tolerance levels of CT number to electron density table for photon beam in radiotherapy treatment planning system J. Appl. Clin. Med. Phys. 19 271–5
- Niu T, Dong X, Petrongolo M and Zhu L 2014 Iterative image-domain decomposition for dual-energy CT Med. Phys. 41 41901
- Papanikolaou N, Battista J, Boyer A, Klein E and Sharpe M 2004 Tissue inhomogeneity corrections for megavoltage photon beams AAPM Task Group-8585 (https://doi.org/10.37206/86)
- Ren L, Chen Y, Zhang Y, Giles W, Jin J and Yin F-F 2016 Scatter reduction and correction for dual-source cone-beam CT using prepatient grids *Technol. Cancer Res. Treat.* 15 416–27
- Sajja S, Lee Y, Eriksson M, Nordström H, Sahgal A, Hashemi M, Mainprize J G and Ruschin M 2020 Technical principles of dual-energy cone beam computed tomography and clinical applications for radiation therapy *Adv. Radiat. Oncol.* 5 1–16
- Samei E, Ranger NT, Dobbins JT and Ravin CE 2011 Effective dose efficiency: an application-specific metric of quality and dose for digital radiography *Phys. Med. Biol.* 56 5099–118
- Schröder L, Stankovic U, Rit S and Sonke J-J 2022 Image quality of dual-energy cone-beam CT with total nuclear variation regularization Biomed. Phys. Eng. Express 8 025012
- Shi L, Bennett N R, Shapiro E, Colbeth R E, Star-Lack J, Lu M and Wang A S 2020a Comparative study of dual energy cone-beam CT using a dual-layer detector and kVp switching for material decomposition *Proc. SPIE Int. Soc. Opt. Eng.* 11312 1131220
- Shi L, Lu M, Bennett N R, Shapiro E, Zhang J, Colbeth R, Star-Lack J and Wang A S 2020b Characterization and potential applications of a dual-layer flat-panel detector *Med. Phys.* 47 3332–43
- Skaarup M, Edmund J M, Dorn S, Kachelriess M and Vogelius I R 2019 Dual-energy material decomposition for cone-beam computed tomography in image-guided radiotherapy *Acta Oncol.* 58 1483–8
- Ståhl F *et al* 2021 Performance characterization of a prototype dual-layer cone-beam computed tomography system *Med. Phys.* 48 6740–54 Tse J J, Dunmore-Buyze J, Drangova M and Holdsworth D W 2018 Dual-energy computed tomography using a gantry-based preclinical
- Wang J, Li T and Xing L 2009 Iterative image reconstruction for CBCT using edge-preserving prior Med. Phys. 36 252-60

cone-beam microcomputed tomography scanner J. Med. Imaging (Bellingham) 5 033503

- Wang W et al 2021 High-resolution model-based material decomposition in dual-layer flat-panel CBCT Med. Phys. 48 6375-87
- Xing L, Thorndyke B, Schreibmann E, Yang Y, Li T-F, Kim G-Y, Luxton G and Koong A 2006 Overview of image-guided radiation therapy Med. Dosim. 3191–112
- Xue Y et al 2021 Multi-material decomposition for single energy CT using material sparsity constraint IEEE Trans. Med. Imaging 40 1303–18 Yamada S, Ueguchi T, Shimosegawa E, Fujino K, Shimazu T, Murase K and Hatazawa J 2015 Feasibility of improved attenuation correction for SPECT reconstruction in the presence of dense materials using dual-energy virtual monochromatic CT: a phantom study Open J. Med. Imaging 05 183–93
- Yang M, Zhu X R, Park P C, Titt U, Mohan R, Virshup G, Clayton J E and Dong L 2012 Comprehensive analysis of proton range uncertainties related to patient stopping-power-ratio estimation using the stoichiometric calibration *Phys. Med. Biol.* 57 4095–115
- Zbijewski W, Gang G, Wang A S, Stayman J W, Taguchi K, Carrino J A and Siewerdsen J H 2013 Noise reduction in material decomposition for low-dose dual-energy cone-beam CT *Proc. SPIE Int. Soc. Opt. Eng.* **8668** 866819
- Zhang Y, Wu H, Chen Z, Knisely J P, Nath R, Feng Z, Bao S and Deng J 2015 Concomitant imaging dose and cancer risk in image guided thoracic radiation therapy *Int. J. Radiat. Oncol. Biol. Phys.* 93 523–31
- Zhang Y, Yan Y, Nath R, Bao S and Deng J 2012a Personalized assessment of kV cone beam computed tomography doses in image-guided radiotherapy of pediatric cancer patients *Int. J. Radiat. Oncol. Biol. Phys.* 83 1649–54
- Zhang Y, Yan Y, Nath R, Bao S and Deng J 2012b Personalized estimation of dose to red bone marrow and the associated leukaemia risk attributable to pelvic kilo-voltage cone beam computed tomography scans in image-guided radiotherapy *Phys. Med. Biol.* 57